LETTER

doi:10.1038/nature11663

Deep penetration of molten iron into the mantle caused by a morphological instability

Kazuhiko Otsuka[1] & Shun-ichiro Karato[1]

The core–mantle boundary of Earth is a region where iron-rich liquids interact with oxides and silicates in the mantle[1]. Iron enrichment may occur at the bottom of the mantle, leading to low seismic-wave velocities and high electrical conductivity[2–5], but plausible physical processes of iron enrichment have not been suggested. Diffusion-controlled iron enrichment is inefficient because it is too slow[6], although the diffusion can be fast enough along grain boundaries for some elements[7]. More fundamentally, experimental studies and geophysical observations show that the core is under-saturated with oxygen, implying that the mantle next to the core should be depleted in FeO. Here we show that (Mg,Fe)O in contact with iron-rich liquids leads to a morphological instability, causing blobs of iron-rich liquid to penetrate the oxide. This morphological instability is generated by the chemical potential gradient between two materials when they are not in bulk chemical equilibrium, and should be a common process in Earth's interior. Iron-rich melt could be transported 50 to 100 kilometres away from the core–mantle boundary by this mechanism, providing an explanation for the iron-rich regions in the mantle.

Like the lithosphere near Earth's surface, the core–mantle boundary region (CMB) of Earth (and other planets) is a region where major physical and chemical actions occur[1]. Some seismological observations suggest the presence of chemical heterogeneity[2–4,8]. Also, anomalously high conductance in some regions of the D′′ layer is inferred from the observed length-of-day variation[9,10]. The regional variations in electrical conductivity observed by geomagnetic jerks (sudden changes in Earth's magnetic field) correspond to regions of anomalous seismic properties[5,11]. Iron enrichment in some regions of the D′′ layer is a plausible explanation of these observations.

However, explaining the iron enrichment is difficult for several reasons. In addition to the difficulties with diffusion-controlled models (because diffusion is so slow), the capillary mechanism of infiltration applies only to a penetration of about 100 m into the mantle or less, owing to the influence of gravity[12]. Iron-rich core materials may infiltrate into the mantle along the pressure gradient caused by the dynamic topography at the CMB[13]. However, the degree of melt penetration by this mechanism is controlled by the amplitude of dynamic topography, which is in turn controlled by the viscosity of the D′′ layer. If we use the viscosity of about 10^{18} Pa s for the D′′ layer[14], the extent of iron penetration for this mechanism is less than a metre, too small to cause any appreciable effects.

Here we report the experimental observations of penetration of iron-rich metallic liquid blobs into the single crystals of (Mg,Fe)O through the morphological instability. The penetration depth of iron-rich blobs observed in these experiments far exceeds the penetration depth attributable to a simple diffusion-controlled model or the other mechanisms discussed above (the capillary mechanism and dynamic topography). Hence, this morphological-instability process is more likely to explain the iron enrichment inferred in some regions of the CMB. We describe our experimental observations, interpret the observations in terms of a physical model, and discuss the possible implications of the deep penetration of molten iron-rich blobs for the properties and dynamics of the D′′ layer.

We conducted high-pressure and high-temperature experiments using a multi-anvil apparatus in which iron-rich liquid and single crystals of (Mg,Fe)O are in direct contact (see Supplementary Information for details). After annealing, we found that each interface between an (Mg,Fe)O crystal and the molten iron was serrated and the liquid metal had penetrated into the (Mg,Fe)O single crystal to form a layer containing many metal-rich blobs (we call this the metal-rich layer, or MRL) (Fig. 1a). The serrated morphology of the metallic liquid and the (Mg,Fe)O interface is characteristic of the morphological instability. Notably, the morphological instability was not observed at the wall of pure MgO single crystals, indicating that the FeO in (Mg,Fe)O plays an essential part in this.

The chemical composition of matrix (Mg,Fe)O changes gradually over the region of liquid penetration (MRL) such that FeO content increases with the distance from the interface (see Fig. 1b). This means that the chemical equilibrium is established only near the interface, and the bulk of the crystals is out of equilibrium.

The characteristic wavelength of the interface morphology measured along the interface is approximately 1–10 μm (Fig. 2). The least-squares fit with $\lambda = k_m L^m$ (where λ is the instability wavelength, L is the thickness of the MRL and k_m and m are constants) gives $m = 0.5 \pm 0.2$ for Fe–$(Mg_{0.45}Fe_{0.55})O$ and 0.3 ± 0.3 for Fe–$(Mg_{0.75}Fe_{0.25})O$.

The thickness of the MRL increases with annealing time, whereas their migration velocity decreases with time (Supplementary Information). The least-squares fit with $L = k_n t^n$ (where t is duration of experiments and k_n and n are constants) gives $n = 0.5 \pm 0.2$. Such a relationship is consistent with a model of MRL growth (see below). Consequently, we may define an effective diffusion coefficient corresponding to the extent of melt migration. The effective diffusivity D_{MRL} was calculated using the equation $D_{MRL} = L^2/t$. Importantly, transcrystalline melt migration is a much more efficient mechanism of chemical transport than the conventional Fe–Mg interdiffusion[15] under most of the conditions investigated.

A morphological instability similar to the one observed in this study has been documented in many systems where two materials sharing one component (FeO in our case) are in contact but chemical equilibrium is attained only near the interface[16]. The concentration gradient of the common component provides the driving force for this instability. The characteristic wavelength at which the instability grows fastest is given by[16]:

$$\lambda = 2\pi\sqrt{3\Gamma C_{eq}^{S}/G} \quad (1)$$

where $\Gamma = \gamma\Omega/RT$ is the capillarity length, C_{eq}^{S} is the equilibrium FeO concentration in solid (Mg,Fe)O and G is the gradient of the FeO concentration (where γ is the liquid–solid interfacial energy, Ω is liquid molar volume and R is the gas constant). Also, the timescale on which the instability grows is given by $\tau \approx \lambda^2/4\pi^2 D$, where D is the Fe–Mg interdiffusion coefficient[16].

The elongated fingers formed at the interface are eventually pinched off (as a result of the surface tension) to produce isolated melt inclusions

[1]Yale University, Department of Geology and Geophysics, 210 Whitney Avenue, New Haven, Connecticut 06511, USA.

©2012 Macmillan Publishers Limited. All rights reserved

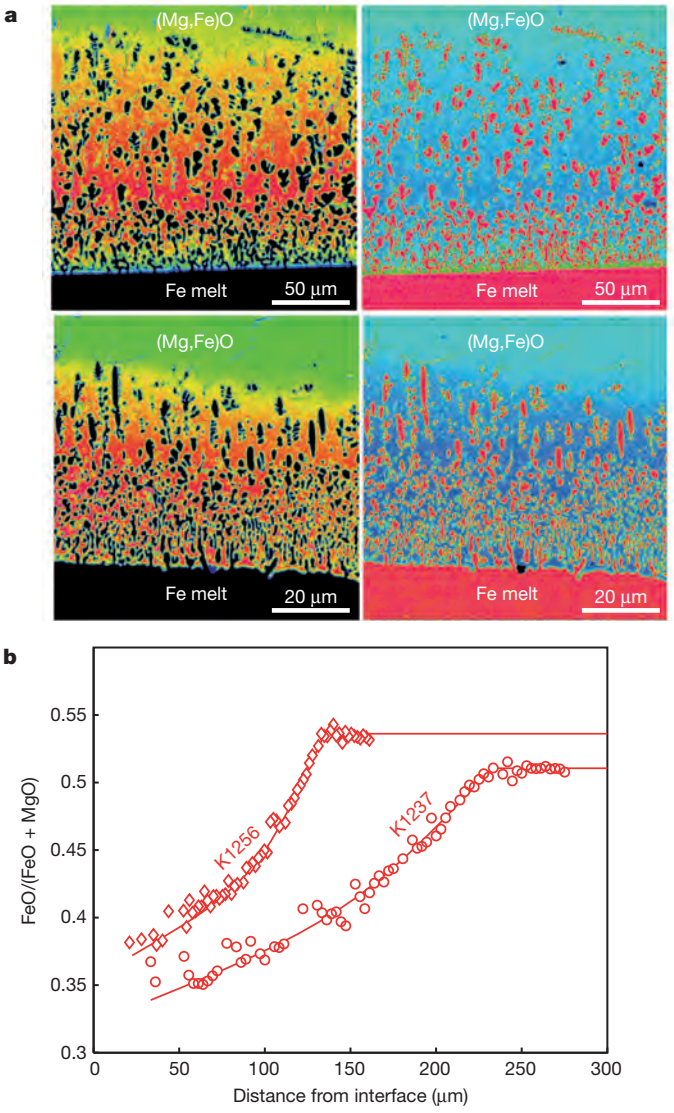

Figure 1 | Distribution of Mg and Fe in the annealed couples of molten Fe and solid (Mg,Fe)O. a, Mapping of Mg concentration (left panels) and Fe concentration (right panels) in molten Fe and solid $(Mg_{0.45}Fe_{0.55})O$ annealed at 2,123 K for 60 s (bottom panels, run number K1234), and in molten Fe and solid $(Mg_{0.45}Fe_{0.55})O$ annealed at 2,123 K for 300 s (top panels, run number K1237). In left panels, red corresponds to high Mg concentration and green corresponds to low Mg concentration. In right panels, red corresponds to high Fe concentration and blue corresponds to low Fe concentration. **b**, Typical iron contents—FeO/(FeO + MgO) in molar ratios—in (Mg,Fe)O over the region of transcrystalline migration of iron-rich liquid inclusions as a function of distance from the melt and solid interface.

(blobs) in the (Mg,Fe)O matrix. The isolated blobs will consume FeO from (Mg,Fe)O at the leading edge, while excess FeO will be precipitated at the another edge. In this way, blobs migrate while they re-establish the gradient of FeO that was initially defined by the degree of disequilibrium and the diffusion coefficients of the relevant species. The analysis summarized in the Supplementary Information shows that the gradient in FeO concentration is approximately given by:

$$G \equiv \frac{dC}{dx} \approx \frac{\Delta C}{L} = \frac{C^S_\infty - C^S_{eq}}{L}$$

where C is the concentration of FeO, x is the distance measured from the interface, C^S_∞ is the FeO concentration in (Mg,Fe)O far from the interface, and C^S_{eq} is the FeO concentration in (Mg,Fe)O that will be in equilibrium with the molten iron. Consequently, the growth of the MRL

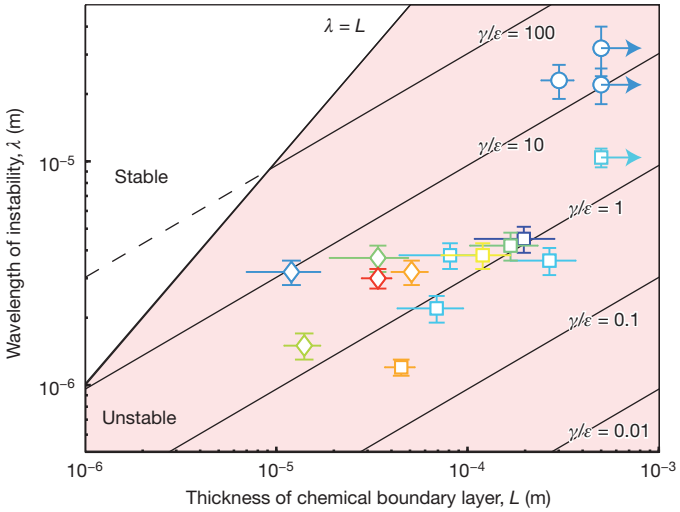

Figure 2 | Instability wavelength λ plotted against thickness of chemical boundary layer *L*. Squares, Fe-$(Mg_{0.45}Fe_{0.55})O$ in MgO capsule; diamonds, Fe-$(Mg_{0.75}Fe_{0.25})O$ in MgO capsule; and circle, MoO_2-$(Mg_{0.75}Fe_{0.25})O$ in Pt/Mo double capsule. Symbol colour indicates experimental temperature, for example from 1,973 K (dark blue) to 2,473 K (red). Arrows pointing right indicate that only the minimum values of the thickness of the chemical boundary layer are constrained. The stability limit of the interface is given here by $\lambda = L$. In the unstable regime, the relation between instability wavelength and the thickness of the chemical boundary layer was estimated using $\lambda = 2\pi\sqrt{3L\Gamma/\varepsilon}\,(\equiv \lambda_{MS})$, where λ_{MS} is the length of the Mullins–Sekerka instability at temperature 2,273 K and pressure 12.5 GPa with the range of γ/ε values from 0.01 to 100. Error bars (both horizontal and vertical) indicate one standard deviation.

follows $dL/dt = A\Delta C/L$, where A is a constant that depends on the mechanism of melt blob migration. Therefore the growth of the MRL is described by:

$$L = \sqrt{A\Delta C t} = \sqrt{D_{MRL} t} \qquad (2)$$

where D_{MRL} $(= A\Delta C)$ is the effective diffusion coefficient.

Our experimental observations also show that D_{MRL} is strongly dependent on temperature, and therefore we use the relation $D_{MRL} = A_0 \Delta C \exp(-E^*/RT)$ to analyse the data (Fig. 3). We found that the activation energy E^* is significantly smaller than that for the interdiffusion coefficient[15,17,18] in (Mg,Fe)O, suggesting that processes other than diffusion control the rate of liquid blob migration. One possibility is control by dissolution–precipitation.

The outer core is predominantly composed of iron-rich molten metal with minor amounts of light elements, including oxygen and silicon[19]. The inferred amount of minor light elements such as oxygen in the outer core is significantly smaller than their solubility in the outer core at the present-day CMB in equilibrium with the normal mantle composition[20]. The degree of supersaturation for (Mg,Fe)O at the base of the mantle is estimated to be $\varepsilon \approx 10$. Using a plausible value (of the order of 1 J m^{-2}) of the interfacial energy, the morphological instability probably occurs at the CMB with a characteristic wavelength of a few centimetres.

To apply our results to the CMB, we need to evaluate the influence of temperature and pressure on the kinetics of MRL growth, because our experiments were conducted at a pressure significantly lower than the CMB pressure[21] (around 135 GPa) and at lower temperatures than the temperature at the CMB[22] (~3,000–4,000 K). We use homologous temperature scaling: $D_{MRL}(T,P) = D_{MRL}(T/T_m(P))$, where $T_m(P)$ is the pressure-dependent melting temperature. For a reasonable value of supersaturation, $\varepsilon \left(\equiv \frac{C^S_\infty - C^S_{eq}}{C^S_{eq}}\right) = 10$, we estimate that the thickness of the MRL is about 50 km after a billion years, and 100 km after 4 billion years. We conclude that melt penetration by the morphological

©2012 Macmillan Publishers Limited. All rights reserved

instability in (Mg,Fe)O is capable of transporting iron-rich core components over tens of kilometres at the base of the lower mantle, affecting the physical and chemical properties of this region.

The upward migration of iron-rich liquid has implications for several aspects of core–mantle interactions. The penetration of iron-rich blobs to tens of kilometres from the CMB can easily explain large velocity reductions and the high electrical conductance of some regions in the D′′ layer. However, the amplitude of velocity anomalies (~2–3%) and the depth extent of the large low-velocity province[1,2] (~200–300 km) may not be consistent with the iron penetration model: the amplitude of velocity reduction is too small and the thickness is too large. Iron penetration may affect physical properties in more localized regions such as a thin layer at the bottom of the large low-velocity province where the concentration of (Mg,Fe)O is large and in small regions with unusually low velocities (see Fig. 4).

Finally, the liquid iron penetrating into the mantle may account for the isotope signatures of the core materials observed in some of the ocean islands[23]. However, processes that could produce such a signature in volcanic rocks erupted at the surface are not well understood. The average density of an iron-rich region is too large for large-scale entrainment to occur by mantle convection[24]. Some small-scale processes, such as flow-induced material segregation[25], would be needed to carry core-affected materials to the surface by a plume. Alternatively, some of the heterogeneities in the D′′ region could be attributed to the remnant of the magma ocean[26] and the pile-up of subducted materials[27].

Some issues remain uncertain and hence require further study. First, in this work we studied coupled iron-rich melt and (Mg,Fe)O. At Earth's CMB, not only (Mg,Fe)O but silicate perovskite or silicate post-perovskite also occur. The penetration depth and the volume fraction of metallic blobs in perovskite (and post-perovskite) will be different in these minerals because of the difference in diffusion coefficient of Fe and the properties that control the blob migration (that is, dissolution–precipitation kinetics). Because iron diffusion in perovskite is much slower than in (Mg,Fe)O (ref. 17), either the density of blobs is lower or the MRL is thinner in perovskite than in (Mg,Fe)O. Consequently, the extent to which iron enrichment occurs at the CMB is probably controlled by the volume fraction of (Mg,Fe)O. When the volume fraction of (Mg,Fe)O exceeds the percolation threshold (about 20%)[28], then substantial penetration of molten iron will occur. Consequently, regional variation in the volume fraction of (Mg,Fe)O will control the extent to which iron enrichment occurs at the CMB.

Further studies are needed to investigate the kinetics of metallic liquid penetration in perovskite (and post-perovskite). The CMB in other planets, such as Mercury, is made of olivine and other low-pressure minerals. A dense layer is inferred to exist in the deep mantle of Mercury[29] that might be caused by the penetration of iron-rich materials into the mantle. Similar studies of olivine and other low-pressure minerals are also important.

Second, the influence of grain boundaries on liquid blob penetration is unknown. Although iron-rich melt does not completely wet the grain boundaries of silicate minerals in most cases[30], complete wetting may occur in (Mg,Fe)O. Gravity will affect the nature of metal penetration if

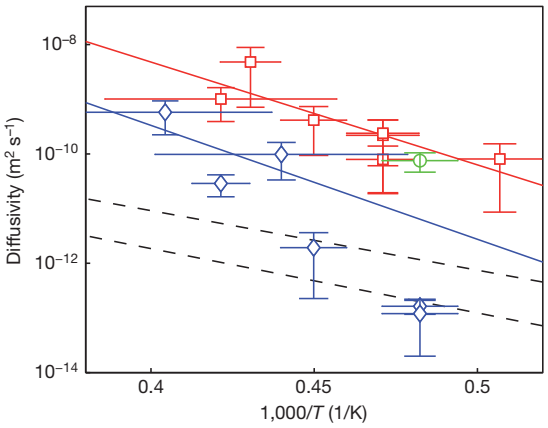

Figure 3 | Effective diffusivity D_{MRL} corresponding to the migration of iron-rich liquid blobs compared with the Fe–Mg interdiffusion coefficient in (Mg,Fe)O. Red squares, Fe–$(Mg_{0.45}Fe_{0.55})O$ in MgO capsule; blue diamonds, Fe–$(Mg_{0.75}Fe_{0.25})O$ in MgO capsule; and green circle, MoO_2-$(Mg_{0.75}Fe_{0.25})O$ in Pt/Mo double capsule. Solid lines indicate the Arrhenius equation $D_{MRL} = (C^S_\infty - C^S_{eq})A_0 \exp[-(E_{Mg}X_{Mg} + E_{Fe}X_{Fe})/RT]$ where E is activation energy, and X is the mole fraction, fitted to the data (colours as for data points). Dashed black lines indicate the Fe–Mg interdiffusion coefficients[18] for $(Mg_{0.45}Fe_{0.55})O$ (top line) and $(Mg_{0.75}Fe_{0.25})O$ (bottom line). Vertical error bars indicate one standard deviation. Horizontal error bars indicate the uncertainties in temperature caused by the temperature gradient or by the thermocouple failure (in the latter case, temperature was estimated using the power–temperature calibration).

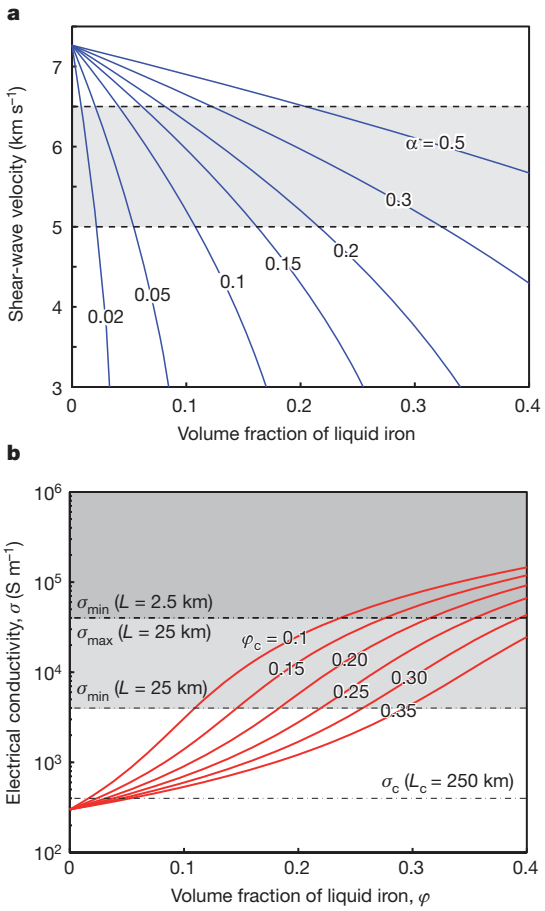

Figure 4 | Influence of liquid iron blobs on geophysically observable properties. **a**, Estimated shear-wave velocity of the silicate/oxide mantle containing the liquid iron. The solid lines are calculated using the oblate spheroid model with aspect ratio α. The shaded region is the range of observed velocities in unusually low-velocity zones. The plausible volume fraction of molten iron is ~0.2–0.3 (see Fig. 1a), and with these values, a reduction of seismic wave velocity of ~10–20% is easily explained with an aspect ratio of 0.2–0.5 (see Fig. 1a). **b**, Electrical conductivity of the silicate/oxide mantle containing the liquid iron. φ_c is the volume fraction of iron-rich melt corresponding to the percolation threshold (representative value is about 0.2). σ_{min} and σ_{max} are the minimum and maximum conductivities corresponding to an assumed layer thickness L that explain the geophysical observations. Inferred ranges of electrical conductivity of a conductive layer at the base of the mantle depend on the thickness of the metal-rich layer, L. The light- and dark-shaded regions represent conductive layers of thickness 25 km and 2.5 km thick, respectively. Again, geophysically inferred conductivity can be explained by the presence of molten iron with a volume fraction of 0.2–0.3.

©2012 Macmillan Publishers Limited. All rights reserved

the iron-rich melt completely wets the grain boundaries. Further studies of the penetration of metallic liquid blobs into polycrystalline and multi-phase materials will help us to understand core–mantle chemical interactions. Finally, the degree of chemical disequilibrium at the CMB probably reflects the chemical history of the CMB and could be heterogeneous, which would cause the observed lateral heterogeneity in the penetration of molten iron into the mantle.

METHODS SUMMARY

All experiments were performed using the Kawai-type multi-anvil press. The (Mg,Fe)O single crystals with a range of FeO content were synthesized at 1,873 K for around 300 h at 0.1 MPa using a high-temperature controlled-oxygen-fugacity furnace. Single crystals of (Mg,Fe)O were annealed together with molten iron at high pressures and temperatures for a range of time (2 to 3,600 s). After each experiment, the sample was quenched by shutting off the furnace at a given pressure and the distribution of elements (Fe and Mg) in recovered samples was determined using a field-emission-gun electron probe microanalyser (JXA-8530F).

Full Methods and any associated references are available in the online version of the paper.

Received 4 June; accepted 3 October 2012.

1. Lay, T., Williams, Q. & Garnero, E. J. The core–mantle boundary layer and deep Earth dynamics. *Nature* **392,** 461–468 (1998).
2. Garnero, E. J. A new paradigm for Earth's core-mantle boundary. *Science* **304,** 834–836 (2004).
3. Trampert, J., Deschamps, F., Resovsky, J. S. & Yuen, D. A. Probabilistic tomography maps chemical heterogeneities throughout the lower mantle. *Science* **306,** 853–856 (2004).
4. Ishii, M. & Tromp, J. Normal mode and free-air gravity constraints on lateral variation in density of Earth's mantle. *Science* **285,** 1231–1236 (1999).
5. Nagao, H., Iyemori, T., Higuchi, T. & Araki, T. Lower mantle conductivity anomalies estimated from geomagnetic jerks. *J. Geophys. Res.* **108,** 2254 (2003).
6. Stevenson, D. J. Models of the Earth's core. *Science* **214,** 611–619 (1981).
7. Hayden, L. A. & Watson, E. B. A diffusion mechanism for core–mantle interaction. *Nature* **450,** 709–711 (2007).
8. Masters, G., Laske, G., Bolton, H. & Dziewonski, A. M. in *Earth's Deep Interior* (eds Karato, S. *et al.*) 63–87 (American Geophysical Union, 2000).
9. Holme, R. Electromagnetic core-mantle coupling. I. Explaining decadal changes in the length of day. *Geophys. J. Int.* **132,** 176–180 (1998).
10. Buffett, B. A. Constraints on magnetic energy and mantle conductivity from the forced nutations of the Earth. *J. Geophys. Res.* **97,** 19581–19597 (1992).
11. Ohta, K. *et al.* Electrical conductivities of pyrolitic mantle and MORB materials up to the lowermost mantle conditions. *Earth Planet. Sci. Lett.* **289,** 497–502 (2010).
12. Poirier, J.-P. & LeMouel, J.-L. Does infiltration of core material into the lower mantle affect the observed geomagnetic field? *Phys. Earth Planet. Inter.* **73,** 29–37 (1992).
13. Kanda, R. V. S. & Stevenson, D. J. Suction mechanism for iron entrainment into the lower mantle. *Geophys. Res. Lett.* **33,** L02310 (2006).
14. Nakada, M. & Karato, S. Low viscosity of the bottom of the Earth's mantle inferred from the analysis of Chandler wobble and tidal deformation. *Phys. Earth Planet. Inter.* **192/193,** 68–80 (2012).
15. Van Orman, J. A., Fei, Y., Hauri, E. H. & Wang, J. Diffusion in MgO at high pressure: constraints on deformation mechanisms and chemical transport at the core-mantle boundary. *Geophys. Res. Lett.* **30,** doi:10.1029/2002GL016343 (2003).
16. Mullins, W. W. & Sekerka, R. F. Stability of a planar interface during solidification of a dilute binary alloy. *J. Appl. Phys.* **35,** 444–451 (1964).
17. Holzapfel, C., Rubie, D. C., Frost, D. J. & Langenhorst, F. Fe-Mg interdiffusion in $(Mg,Fe)SiO_3$ perovskite and lower mantle. *Science* **309,** 1707–1710 (2005).
18. Yamazaki, D. & Irifune, T. Fe-Mg interdiffusion in magnesiowüstite up to 35 GPa. *Earth Planet. Sci. Lett.* **216,** 301–311 (2003).
19. Anderson, O. L. & Isaak, D. G. Another look at the core density deficit of Earth's outer core. *Phys. Earth Planet. Inter.* **131,** 19–27 (2002).
20. Frost, D. J. *et al.* Partitioning of oxygen between the Earth's mantle and core. *J. Geophys. Res.* **115,** doi:10.1029/2009JB006302 (2010).
21. Dziewonski, A. M. & Anderson, D. L. Preliminary reference Earth model. *Phys. Earth Planet. Inter.* **25,** 297–356 (1981).
22. Boehler, R. Temperatures in the Earth's core from melting point measurements of iron at high static pressures. *Nature* **363,** 534–536 (1993).
23. Brandon, A. & Walker, R. J. The debate over core-mantle interaction. *Earth Planet. Sci. Lett.* **232,** 211–225 (2005).
24. Sleep, N. H. Gradual entrainment of a chemical layer at the base of the mantle by overlying convection. *Geophys. J. R. Astron. Soc.* **95,** 437–447 (1988).
25. Leighton, D. & Acrivos, A. The shear-induced migration of particles concentrated suspensions. *J. Fluid Mech.* **181,** 415–439 (1987).
26. Labrosse, S., Hernlund, J. W. & Coltice, N. A crystallizing dense magma ocean at the base of the Earth's mantle. *Nature* **450,** 866–869 (2007).
27. McNamara, A. K., Garnero, E. & Rost, S. Tracking deep mantle reservoirs with ultra-low velocity zones. *Earth Planet. Sci. Lett.* **299,** 1–9 (2010).
28. Stauffer, D. & Aharony, A. *Introduction to Percolation Theory* (Taylor and Francis, 1992).
29. Smith, D. E. *et al.* Gravity field and internal structure of Mercury from MESSENGER. *Science* **336,** 214–217 (2012).
30. Shannon, M. C. & Agee, C. B. Percolation of core melts at lower mantle conditions. *Science* **280,** 1059–1061 (1998).

Supplementary Information is available in the online version of the paper.

Acknowledgements We are grateful to Z. Du, T. Hiraga, T. Kawazoe, K. Tsuno and T. Yoshino for discussions and J. Eckert, G. Amulele, Z. Du, D. Wang and R. Farla for technical support. We thank M. Zuber, J. Schubert and S. Peale for a discussion on Mercury. B. Buffett provided a useful comment on the magnetic coupling between the core and the mantle. B. Watson provided constructive criticism. This research was financially supported by the National Science Foundation under grant number EAR-0809330.

Author Contributions Experimental studies were conducted by K.O. Theoretical interpretation and geophysical applications were done by both K.O. and S.K. Both authors wrote the paper.

Author Information Reprints and permissions information is available at www.nature.com/reprints. The authors declare no competing financial interests. Readers are welcome to comment on the online version of the paper. Correspondence and requests for materials should be addressed to S.K. (shun-ichiro.karato@yale.edu).

©2012 Macmillan Publishers Limited. All rights reserved

METHODS

Starting materials consisted of single crystals of (Mg,Fe)O and reagent-grade Fe metal or MoO_2 powder. (Mg,Fe)O crystals were synthesized by annealing MgO crystals embedded in the mixtures of MgO and Fe_2O_3 haematite powder in a gas-mixing furnace at temperature of 1,873 K and at an oxygen fugacity of 1 Pa for approximately 300 h as described in ref. 31. The chemical analysis of two sets of recovered samples by a field-emission-gun electron probe micro-analyser (JXA-8530F) showed that the molar Mg/(Mg + Fe) ratio ranged between 0.45 and 0.50 and between 0.75 and 0.80 for each crystal and varied less than 1% over the sample size used for high-pressure, high-temperature experiments. We refer to those compositions as $(Mg_{0.45}Fe_{0.55})O$ and $(Mg_{0.75}Fe_{0.25})O$, respectively. Those crystals were drilled into cylindrical shapes with thicknesses from 0.5 to 0.8 mm and diameters of 1.1 mm with the cylindrical axis oriented close to the [100] crystallographic direction.

High-pressure and high-temperature experiments were performed using a 1,000-ton Kawai-type multi-anvil apparatus. Tungsten carbide cubes with the truncation edge length of 8 mm or 11 mm were used as second-stage anvils. The octahedral edge-length of the Cr_2O_3-doped MgO pressure medium was either 14 mm or 18 mm for the 14/8 and 18/11 assemblies, respectively. The pressure–load relationship for these cell assemblies were calibrated as described in ref. 32. The cross-section of the cell assembly is shown in Supplementary Fig. 1. For the 14/8 assembly, one single crystal of synthetic ferropericlase was packed with Fe powder in a sample capsule made of single crystals of MgO with inner diameter 1.7 mm and outer diameter 2.6 mm. The sample capsule was directly inserted to a stepped $LaCrO_3$ furnace. For an 18/11 assembly, one (Mg,Fe)O crystal was packed with MoO_2 powder in an outer Pt and inner Mo double capsule with inner diameter 1.6 mm and outer diameter 2.0 mm. The double capsule was insulated from a stepped graphite furnace by a MgO cylinder. For both assemblies, the cylindrical axis of the sample capsule was vertically aligned with gravity to avoid gravitational rearrangement during annealing. Temperature was monitored with a $W_{95}Re_5$–$W_{74}Re_{26}$ thermocouple with a thermocouple junction placed in contact with one end of the sample capsule without correcting for the effect of pressure on electromotive force. The ceramic parts of the cell assemblies were fired at approximately 1,000 K overnight before assemblage and kept in a vacuum oven at approximately 400 K.

In each experiment, the starting material was brought up to pressure by raising the load at room temperature. Subsequently, temperature was raised by applying current across the furnace at two different heating rates: first at a rate of 50 K min^{-1} up to 1,873 K, close to the eutectic temperature in the Fe–FeO system[33,34], and later at a much higher rate, usually 100–200 K min^{-1} (or even higher), up to the target temperature to minimize possible chemical reactions between (Mg,Fe)O and metallic iron during heating. For a 14/8 cell assembly, the resistance of the $LaCrO_3$ furnace occasionally dropped during heating at around 1,823–1,873 K owing to the leakage of molten Fe from the MgO capsule, which caused very rapid temperature ramp-up at rates of 400–1,000 K min^{-1} in the voltage-controlled heating system. Experimental durations were typically of the order of seconds to hours depending on the speed of melt migration. The samples were then quenched isobarically by shutting off the heating power and subsequently decompressed at room temperature. Experimental conditions are typically pressure 12.5 GPa and temperature 1,973–2,373 K.

31. Otsuka, K., McCammon, C. & Karato, S. Tetrahedral occupancy of ferric iron in (Mg,Fe)O: implications for point defects in the Earth's lower mantle. *Phys. Earth Planet. Inter.* **180,** 179–188 (2010).
32. Otsuka, K. & Karato, S. Control of the water fugacity at high pressures and temperatures: applications to the incorporation mechanisms of water in olivine. *Phys. Earth Planet. Inter.* **189,** 27–33 (2011).
33. Ringwood, A. E. & Hibberson, W. The system Fe-FeO revisited. *Phys. Chem. Miner.* **17,** 313–319 (1990).
34. Seagle, C. T., Heinz, D. L., Campbell, A. J., Prakapenka, V. B. & Wanless, S. T. Melting and thermal expansion in the Fe-FeO system at high pressure. *Earth Planet. Sci. Lett.* **265,** 655–665 (2008).

©2012 Macmillan Publishers Limited. All rights reserved

Supplementary Information

S1. Experimental methods and observations

High-pressure annealing experiments were conducted using the Kawai-type multi-anvil apparatus. The cell assembly is shown in **Fig. S1.** The details of experimental procedure are given in **Methods**. All the data are summarized in Table S1. After the experiments, the retrieved samples were mounted in epoxy resin and polished for textural analysis using a scanning electron microscope (XL30 ESEM-FEG). Typical back-scattered electron images of run products are shown in **Fig. S2**. Quenched iron-rich metal surrounding the (Mg,Fe)O crystal consists of aggregates of small oxide-rich blobs and dendrites (e.g., 1-10 μm in diameter) in the iron-rich matrix. Those blobs and dendrites were interpreted to have exsolved during the temperature quench from the Fe-rich metallic liquid dissolving oxygen homogeneously. Similar phenomenon was noted in the previous work and the constituents of blobs and matrix were identified as wüstite and α-iron[5]. There is a nearly blob-free zone, approximately 30-100 μm wide, adjacent to the liquid/solid interface where exolved oxide precipitated at the interface. The bulk compositions of iron-oxide liquid were estimated by integrating the compositions of the metal matrix and the oxide blobs based on their volume fractions[5]. The estimated oxygen concentration ranges from 0.8 to 1.6 wt% **(Table S1).**

The instability wavelength (average distance of instability fingers) was measured by counting the number of instability fingers along a line approximately 10 μm away from the liquid/solid interface in order to avoid the influence of oxide exsolution during the quench. The volume fraction of iron-rich liquid inclusions in the (Mg,Fe)O matrix

was determined by analyzing the back-scattered electron images using Photoshop^{TM}. The average values of wave-length of instability and liquid fraction are reported in **Table S1.** The penetration depth of blobs increases with the annealing time while their migration velocity decreases with time **(Fig. S3).** The least squares fit with $L = kt^n$ [where t is duration of experiments and k and n are constants] gives n ranging from 0.6±0.2 for Fe-$(Mg_{0.45}Fe_{0.55})O$ at 2123 K and 0.4 for Fe-$(Mg_{0.75}Fe_{0.25})O$ at 2073 K.

The composition of each run product was analyzed by an electron probe micro-analyzer (JXA-8530F). The following elements were analyzed by WDS (wave-length dispersive spectroscopy) with the standards in the brackets: Fe (Fe_2O_3 for oxide and Fe metal for metal), Mg (MgO), Mo (Mo metal). The analytical condition was typically an acceleration voltage of 15 kV and a beam current of 15 nA with a focused electron beam with the measurement time of 20 seconds at the peak wavelength and 10 s at the both sides of the background. Chemical compositions of matrix (Mg,Fe)O over the region of melt migration were measured along the lines perpendicular to the liquid/solid interface in steps of about 1-2 μm. Note that the iron-rich liquid inclusions have exsolution rim enriched in iron oxide. Measurements were avoided near iron-rich liquid inclusions (approximately ~2 μm away from inclusions). Measurements that are obviously influenced by oxide exsolution were discarded. Observed profiles were shown in **Fig. 1e**. Typically the composition of (Mg,Fe)O changes monotonously over the region containing liquid inclusions. The slope of concentration gradient apparently increases gradually with the distance from the melt/solid interface increases. Time-studies show that the concentration gradient decreases with annealing time over the region of trans-crystalline migration of liquid inclusions. The degree of super-saturation ε was estimated

using the equation $\varepsilon = \frac{C_{\infty}^{S} - C_{Eq}^{S}}{C_{Eq}^{S}}$ where C_{Eq}^{S} is F eO concentration of (Mg,Fe)O at the interface with Fe-rich liquid and C_{∞}^{S} is the FeO concentration in (Mg,Fe)O far away from the liquid interface (initial FeO concentration). C_{Eq}^{S} and C_{∞}^{S} are listed in **Table S1.** Estimated σ was found to be almost independent of experimental conditions, giving the average value of 0.6±0.2.

S2. A model of penetration of liquid metal blobs into the oxide

Consider a pair of material that has a common component (solute atoms (molecules)). At the interface, the concentration of the common component must be at the equilibrium value. However, if the time-scale of a phenomenon we consider is shorter than the diffusion time-scale corresponding to the size of the system, the concentration of the common component away from the interface is out of equilibrium. Consequently, the diffusional flow of solute atoms occurs from one side to another, and the interface migrates with a velocity, V, given by[6]

$$V = \frac{D}{C_{Eq}^{S} - C_{Eq}^{L}} G_c = \frac{D}{C_{Eq}^{S} - C_{Eq}^{L}} \left(\frac{\partial C}{\partial x} \right) \qquad \text{(S1)}$$

where D is the diffusion coefficient of the solute, $C_{Eq}^{S,L}$ is the concentration of the solute (in the solid and liquid respectively), FeO, in (Mg,Fe)O (molten iron) at the interface, and $G_c (= \left(\frac{\partial C}{\partial x} \right))$ is the concentration gradient of the solute (FeO) that will be calculated

based on the mass conservation consideration when a metal-rich layer (MRL) grows (see the later part of this section).

Mullins and Sekerka[7,8] showed that, in such a case, the morphological instability will occur on the moving interface for the perturbation with the larger than a critical value viz.,

$$\lambda > \lambda_c = 2\pi\sqrt{\frac{\Gamma}{1-K}\frac{D}{V}} \qquad \text{(S2)}$$

where λ_c is the critical wavelength above which the instability occurs, K is the partition coefficient of the solute between the two phases ($K = \frac{C_{Eq}^{L}}{C_{Eq}^{S}}$). We consider a case where the liquid phase migrates into the solid phase, and Γ is the capillary length determined by the interfacial energy as $\Gamma = \frac{\gamma\Omega}{RT}$ (γ : the interfacial energy between the solid and the liquid). The wavelength of the fastest growing perturbation is given by $\lambda_{MS} = \sqrt{3}\lambda_c$ and therefore the characteristic time for the growth of instability is given by

$$\tau_{MS} \approx \frac{\lambda_{MS}^2}{4\pi^2 D} \approx \frac{3}{1-K}\frac{\Gamma}{V} = \frac{3C_{Eq}^{S}\Gamma}{DG_c} \qquad \text{(S3)}$$

Note that the wavelength of instability can also be written in terms of degree of super-saturation as

$$\lambda_{MS} = 2\pi\sqrt{\frac{3L\Gamma}{\varepsilon}} = 2\pi\sqrt{\frac{3L\gamma\Omega}{\varepsilon RT}} \qquad \text{(S4)}$$

where we define $\varepsilon = \frac{C_{\infty}^{S} - C_{Eq}^{S}}{C_{Eq}^{S}}$ as a measure of super-saturation (disequilibrium). Equation (S4) is used in **Fig. 2** where we compare the experimental observations of the length scale of instability with the Mullins-Sekerka theory.

The application of the Mullins-Sekerka theory to our case has a minor detail. In our case, we consider the interaction of liquid iron with (Mg,Fe)O, oxygen being the common component. Also, the oxygen content in the liquid phase (molten iron) is smaller than the equilibrium oxygen content corresponding to the bulk oxygen content of (Mg,Fe)O. Therefore, oxygen diffuses into the molten iron. However, because of the charge neutrality requirement, the diffusion of oxygen must be accompanied with the diffusion of cation. Because Mg solubility is very low in the molten iron, iron ion will be dissolved into iron together with oxygen. Consequently, due to the bulk disequilibrium near the boundary, FeO is removed from (Mg,Fe)O to molten iron, leaving FeO depleted regions in (Mg,Fe)O near the interface. Therefore we can consider FeO rather than oxygen as a "solute" in our formulation, and the diffusion coefficient that appears in the above equations should be interpreted as the chemical diffusion coefficient of FeO in (Mg,Fe)O.

When the perturbation grows, then the surface tension will pinch off and an isolated blob will be formed. The formation of the Mullins-Sekerka instability is caused by the gradient of composition of the solute, FeO. As far as the gradient in the concentration of FeO is present, the blobs will migrate due to the dissolution at the front and precipitation at the back. The concentration of FeO is, however, modified by the penetration of iron-rich blobs. The amount of FeO exchange depends also on the volume

fraction of the blobs. Therefore, we need to consider the processes by which the volume fraction of the blobs is controlled and the processes by which FeO exchange occurs at the leading edge of the MRL.

Now we should also consider the FeO exchange at the leading edge of the blob-rich region. The MRL moves into the (Mg,Fe)O by which both iron-rich blobs and (Mg,Fe)O matrix will move into (Mg,Fe)O with different concentration gradient of FeO. During its motion, the concentration of FeO in (Mg,Fe)O next to iron-rich blobs is in chemical equilibrium with iron-rich blobs because the mean distance of iron-rich blobs (a few μm) is, in most cases, smaller than the characteristic length of diffusion. Consequently, the front of the MRL moves with a velocity of the migration of iron-rich blobs, $\upsilon\left(=AG_c\right)$, and the concentration profile of FeO in front of the moving MRL is given by

$$C^S = C^S(0) + B\left[1-\exp\left(-\frac{\upsilon}{D}x\right)\right] \qquad \text{(S5)}$$

where the origin of x is at the front of the MRL, and $B = C_\infty^S - C_{Eq}^S - LG_c$ ($C^S(0) = C_{Eq}^S + LG_c$). This gives

$$\left(\frac{\partial C}{\partial x}\right)_o = \left(C_\infty^S - C_{Eq}^S - LG_c\right)\frac{\upsilon}{D}. \qquad \text{(S6)}$$

Because this slope is in general different from G_c, there is mass exchange at this front (**Fig. S4**). We may analyze the mass exchange at this front in two steps. Let us first

consider a process where iron-rich blobs migrate into the metal-free (Mg,Fe)O region by Δx, where blobs replace (Mg,Fe)O without the exchange of FeO. Then we consider the exchange of FeO between iron blobs and nearby (Mg,Fe)O to assure chemical equilbrium. Between these processes, the amount of FeO in the system should be unchanged. This leads to

$$G_c = \frac{C_\infty^S - C_{Eq}^S}{L} - \frac{D}{AL}\frac{1-\phi+K\phi}{1-\phi} \tag{S7}$$

This relation means that the driving force is small as the volume fraction of the blobs is large. And at a certain volume fraction it will vanish, $G_c = 0$, and the melt penetration will stop. This condition is met when the liquid fraction satisfies

$$\phi_c = \frac{\frac{A\left(C_\infty^S - C_{Eq}^S\right)}{D} - 1}{K + \frac{A\left(C_\infty^S - C_{Eq}^S\right)}{D} - 1}. \tag{S8}$$

Our experimental observations show $\frac{A\left(C_\infty^S - C_{Eq}^S\right)}{D} = 10 - 100$ and for K~0.1 (these values are similar under more realistic CMB conditions), we obtain ϕ_c~1. For all our experiments (as well as in real Earth as we discuss later), $\phi \ll \phi_c$ and $\frac{C_\infty^S - C_{Eq}^S}{L} \gg \frac{D}{AL}\frac{1-\phi+K\phi}{1-\phi}$. Consequently,

$$G_c \approx \frac{C_\infty^S - C_{Eq}^S}{L} \tag{S9}$$

The above analysis shows that the gradient in chemical composition in the MRL is roughly controlled by the degree of super-saturation (dis-equilibrium). Therefore, the growth kinetics of the MRL follows

$$\upsilon = \frac{dL}{dt} \approx A\frac{C_{\infty}^{S} - C_{Eq}^{S}}{L} \qquad \text{(S10)}$$

and

$$L = \sqrt{A\left(C_{\infty}^{S} - C_{Eq}^{S}\right)t}\ . \qquad \text{(S11)}$$

Now let us consider how the volume fraction of iron-rich bobs is determined. From the geometry shown in **Fig. S4**, we have

$$\phi = \left(\frac{a}{c}\right)^2 \frac{b}{d} = \frac{1}{\beta^2 \xi} \qquad \text{(S12)}$$

where *a, b, c, d* are defined in Fig. S4, and $b = \alpha a$, $c = \beta a$ and $d = \xi b$. The parameter β is controlled by the kinetics of Mullins-Sekerka instability and for simplicity we assume $\beta \approx 1$ and $\alpha \approx 1$, leading to $\phi \approx \frac{1}{\xi} = \frac{a}{d}$.

The mean distance between two adjacent blobs, *d*, is controlled by the ratio of time scales of nucleation of instability and the time scale of blob migration. Namely, during the time interval when a blob migrates a distance *d*, a new blob must be formed at the interface. This leads to the following relation,

$$\frac{d}{\upsilon} \approx \tau_{MS} = \frac{3}{1-K}\frac{\Gamma}{V} \qquad \text{(S13)}$$

where τ_{MS} is the characteristic time for the Mullins-Sekerka instability and υ is the migration velocity of a blob (equation (S10)). From equation (S13), we have $\xi = \frac{d}{a} = \frac{3A}{D}\frac{C_{Eq}^{S}\Gamma}{a} = \frac{3}{2\pi}\frac{AC_{Eq}^{S}}{D}\sqrt{\frac{\varepsilon\Gamma}{L}}$, and hence

$$\phi = \frac{2\pi}{3}\frac{D}{AC_{Eq}^{S}}\sqrt{\frac{L}{\Gamma\varepsilon}} \ . \qquad \text{(S14)}$$

This result suggests that the volume fraction of liquid-filled blobs increases with the thickness of the MRL (because with the increase of the thickness, the driving force for instability decreases and hence the blob size increases). Eventually, the volume fraction reaches the percolation threshold ($\phi_{thre} \approx 0.2$ [9]) at which the volume fraction will no longer increase because Fe-rich melt will sink due to gravity. Consequently, even if the volume fraction increases with the layer thickness (i.e., with time), the volume fraction of the blobs will always remain just below the percolation threshold and is far less than the critical volume fraction defined by equation (S8), and the relation (S9) will also hold[1].

S3. Influence of gravity

[1] It should be noted that the relation (S13) is derived under the simplifying assumptions of $\beta \approx 1$ and $\alpha \approx 1$ that may not be valid. Consequently, relation (S14) may not be valid if these simplifying assumptions are not satisfied.

Influence of gravity on the Fe-rich melt penetration becomes important when the characteristic length of iron-rich region (i.e., the blob size) becomes large. For instance, the shape of a liquid blob in the gravitational field is controlled by the competition between surface tension and gravity and blob is stable only below a critical size given by[10,11]

$$R_c \approx \sqrt{\frac{\gamma}{\Delta\rho \cdot g}} \qquad \text{(S15)}$$

where γ is the interfacial energy, g is the acceleration due to gravity and $\Delta\rho$ is the density difference between the blob and the surrounding material. Inserting typical values, one obtains $R_c \approx$ 1 cm. Because the typical blob size in the lab and in Earth is less than or comparable to ~1 cm, the influence of gravity on the shape of a blob is negligible.

Gravity may also contribute to the separation of a blob from the matrix. Using the Stokes formula for the sinking velocity, $\upsilon_S = \frac{2}{9}\frac{ga^2\Delta\rho}{\eta}$, where a is the blob size, $\Delta\rho$ is the density difference between a sinking blob and the matrix, and η is the viscosity of the matrix. In order for gravitational separation be efficient, the size of blobs need to be larger than

$$a > \sqrt{\frac{9}{2}\frac{L\eta}{\Delta\rho \cdot g \cdot t_g}} \qquad \text{(S16)}$$

where t_g is the geological timescale (~10^{16} s). For a range of viscosity of the mantle materials ($\eta \approx 10^{18}$-10^{22} Pas[12,13]) and L=10 km, the size of the blob needs to be larger than 10-1000 m for efficient gravitational separation. The initial blob size controlled by the Mullins-Sekerka instability will be ~1 cm for the geological timescale. Possible subsequent growth caused by grain-growth is also limited to ~1 cm according to the experimental and theoretical studies of grain-growth[14,15]. Therefore we consider that the influence of gravity is negligible.

Gravity may also affect the characteristic length of the Mullins-Sekerka instability (i.e., the size of iron-rich blobs). In the Mullins-Sekerka theory, the size of a blob is controlled by the competition between bulk free energy change (caused by the super-saturation with the impurity, FeO in our case) and the change in the free energy due to surface tension (see equation (S4)). Gravity will provide contribution to reduce the tendency for instability in addition to surface tension. An order of magnitude estimate of these two effects shows that these two effects will be comparable if the blob size is ~ 1 cm. The blob size estimated without the influence of gravity is ~ 1 cm under the deep mantle conditions. Consequently, the influence of gravity is to increase the blob size somewhat but not much, and therefore the gravity would not substantially modify the major conclusions of our work. However, we note that the energy change due to surface tension and gravity has different dependence on the size of a perturbation, and therefore the influence of gravity may modify the details of the nature of the Mullins-Sekerka instability. This topic will be analyzed in the forthcoming paper.

S4. Influence of molten iron-rich blobs on seismic wave velocities and electrical conductivity

Seismic wave velocities of the solid and liquid mixtures strongly depend on the structural factors including liquid volume fraction and the geometry of liquid containing space[16,17]. In our experiments, liquid blobs show nearly ellipsoidal shape, but in a more realistic case, liquid layer along grain-boundaries must also be included. Because the relative contributions from these different liquid-containing regions is unknown, we show the influence of metallic liquids on seismic wave velocities corresponding to various melt morphologies (aspect ratios) using the theory by O'Connell and Budianski[16]. **Fig. 4a** in the text shows the results. We employed the values of preliminary reference Earth model (PREM[18]) as our end-member (liquid-free) velocities. It is seen that if more than 10% of liquid iron is present, as seen in our experiments, then the reduction of shear wave velocity by ~10-20 % can be easily attributed to the presence of iron-rich liquid. However, the exact amount of velocity reduction due to the molten iron-rich blobs depends strongly on the geometry of liquid iron.

Similarly, electrical conductivity of the composite strongly depends on connectivity of the conducting phase. As an illustration of the effect of liquid iron fraction and its geometry on electrical conductivity, we estimated the electrical conductivity of mixtures of the silicate/oxide mantle and the liquid iron using the general effective media model[19]. In this model, a parameter called the critical volume fraction determines the percolation threshold. The critical volume fraction of composites is approximately 0.16 when conducting hard spheres are placed at random on a regular lattice or when they are randomly packed with nearly equal sized insulating spheres. In

general, the critical volume fraction varies between 0.01 and 0.6 in various composite media[19]. We employed the values of electrical conductivity of ambient silicate/oxide and liquid iron as 10^2 S/m based on the experimental data by Xu et al.[20] (we consider the influence of high temperature at the D" layer) and 10^6 S/m[21], respectively. Two observational constrains were given for the electrical conductivities of a conducting layer in the lower mantle. First, core-mantle magnetic coupling inferred from the Earth's nutation constrains the minimum conductance of 10^8 S[22,23]. Second, the magnetic diffusion time should not be less than one year in order not to screen time variations in the magnetic field (Buffet, personal communication, 2012). Those two constrains give the lower and upper bound of as 10^4 S/m (10^5 S/m) and 3×10^5 S/m (3×10^7 S/m), respectively, for a 10 km (1 km) thick conductive layer. The results of calculations are shown in **Fig. 4b**. Again with a plausible volume fraction of metallic blobs (close to the percolation threshold, ~0.2), it is possible to explain such high conductivity. However, the magnitude of increase in conductivity depends strongly on the geometry of the iron-rich materials.

Figure S1. Cross-section of a multi-anvil cell assembly

The pressure medium consists of Cr-doped MgO, $LaCrO_3$ heater, ZrO_2 insulating sleeve and $W_{95}Re_5$-$W_{74}Re_{26}$ thermocouple. The cylindrical axis of the sample capsule was vertically aligned with gravity.

Figure S2. Back-scattered electron images of run products

(a) Fe-$(Mg_{0.45}Fe_{0.55})O$ at 2123 K for 60 seconds (K1234), (b) Fe-$(Mg_{0.45}Fe_{0.55})O$ at 2123 K for 3600 seconds (K1230), (c) is the expansion of the rectangular area in (b), (d) Fe-$(Mg_{0.45}Fe_{0.55})O$ at 2373 K for 2 seconds (K1232), (e) Fe-$(Mg_{0.75}Fe_{0.25})O$ at 2073 K for 1200 seconds (K1249), (f) Fe-$(Mg_{0.75}Fe_{0.25})O$ at 2373 K for 90 seconds (K1248). The rectangular area of (a) indicates the area of elemental mapping shown in Fig. 1.

Figure S3. Time series of penetration depth of melt inclusions

(a) Fe-$(Mg_{0.45}Fe_{0.55})O$ at 2123 K for 30 seconds (K1256), 60 seconds (K1234) and 300 seconds (K1237) and (b) Fe-$(Mg_{0.75}Fe_{0.25})O$ at 2073 K for 300 seconds (K1243) and 1200 seconds (K1249). The least squares fit with $L = kt^n$ [where t is duration of experiments and k and n are constants] gives n ranging from 0.6±0.2 for (a) and 0.4 for (b).

Figure S4. A schematic of the structure of melt-rich layer

The iron-rich melt penetrates into the oxide ((Mg,Fe)O) at the interface (the core-mantle boundary) due to the morphological instability caused by the bulk dis-equilibrium between iron-rich melt and oxide (mantle). When instability grows to some extent, surface tension pinches off the liquid region to form isolated blobs. These blobs migrate

through the oxide or silicate ((Mg,Fe)O in this case) because of the presence of the gradient in FeO concentration caused by the bulk dis-equilibrium. At the front of moving metal-rich layer (MRL), exchange of FeO occurs. The gradient in FeO concentration, the driving force for metallic liquid blob migration is determined by the mass balance at this front. An inset shows a schematic diagram from which the volume fraction of liquid blobs can be calculated.

Table S1: Experimental conditions and results

Run	Cell	P [GPa]	T [K]	dK/dt [K/min]	t [s]	L [μm]	λ [μm]	F [%]
$(Mg_{45}Fe_{65})O$-Fe in MgO capsule								
K1239	14/8	12.5	1973±50	100	480	197±88	4.5±0.6	31±1
K1256	14/8	12.5	2123±50	125	30	81±37	3.8±0.5	29±2
K1234	14/8	12.5	2123±50	125	60	69±26	2.2±0.3	33±3
K1237	14/8	12.5	2123±50	250	300	268±100	3.6±0.5	32±6
K1230	14/8	12.5	2123±50	250	3600	>500	10.4±1.0	35±3
K1257	14/8	12.5	2223±50	>400	68	168±65	4.2±0.6	25±3
K1254	14/8	12.5	2223±50	>1000	3	120±47	3.8±0.5	29±3
K1232	14/8	12.5	2373±200	>400	2	45±8	1.2±0.1	50±3
$(Mg_{75}Fe_{25})O$-Fe in MgO capsule								
K1243	14/8	12.5	2073±50	80	300	7±1	n.d.	23±3
K1249	14/8	12.5	2073±50	>400	1200	12±5	3.2±0.4	29±6
K1260	14/8	12.5	2223±50	500	600	34±15	3.7±0.5	29±1
K1247	14/8	12.5	2273±200	>400	2	14±3	1.5±0.2	25±5
K1248	14/8	12.5	2373±50	1200	90	51±11	3.2±0.4	22±2
K1244	14/8	12.5	2473±200	>400	2	34±6	3±0.3	31±2
$(Mg_{75}Fe_{25})O$-MoO_2 in Pt/Mo double capsule								
K1108	18/11	5	2073±50	50	1200	301±58	23±4	21±2
K1107	18/11	5	2073±50	50	3600	>500	32±8	20±1
K998	14/8	15	2073±50	50	7200	>500	22±4	18±1

Note: dK/dt: temperature ramp-up rate from 1600 ºC to a target temperature; L: penetration depth of liquid instability spacing; F: volume fraction of liquid inclusions in ferropericlase matrix; C_O: oxygen concentrati surruinding ferropericlase; $C^S_{Eq\ FeO}$: FeO contents [FeO/(MgO=FeO)] in ferropericlase at the liquid/solid in

1 Otsuka, K., McCammon, C. & Karato, S. Tetrahedral occupancy of ferric iron in (Mg,Fe)O: Implications for point defects in the Earth's lower mantle. *Physics of the Earth and Planetary Interiors* **180**, 179-188 (2010).

2 Otsuka, K. & Karato, S. Control of the water fugacity at high pressures and temperatures: Applications to the incorporation mechanisms of water in olivine. *Physics of the Earth and Planetary Interiors* **189**, 27-33 (2011).

3 Ringwood, A. E. & Hibberson, W. The system Fe-FeO revisited. *Physics and Chemistry of Minerals* **17**, 313-319 (1990).

4 Seagle, C. T., Heinz, D. L., Campbell, A. J., Prakapenka, V. B. & Wanless, S. T. Melting and thermal expansion in the Fe-FeO system at high pressure. *Earth and Planetary Science Letters* **265**, 655-665 (2008).

5 Asahara, Y., Frost, D. J. & Rubie, D. C. Partitioning between magnesiowüstite and liquid iron at high pressures and temperatures: Implications for the composition of the Earth's outer core. *Earth and Planetary Science Letters* **257**, 435-449 (2007).

6 Sekerka, R. F. Application of the time dependent theory of interface stability to an isothermal phase transformation. *Journal of Physics and Chemistry of Solids* **28**, 983-994 (1967).

7 Mullins, W. W. & Skerka, R. F. Morphological stability of a particle growing by diffusion or heat flow. *Journal of Applied Physics* **34**, 323-329 (1963).

8 Mullins, W. W. & Skerka, R. F. Stability of a planar interface during solidification of a dilute binary alloy. *Journal of Applied Physics* **35**, 444-451 (1964).

9 Stauffer, D. & Aharony, A. *Introduction to Percolation Theory*. (Taylor and Francis, 1992).

10 Karato, S. & Murthy, V. R. Core formation and chemical equilibrium in the Earth I. physical considerations. *Physics of Earth and Planetary Interiors* **100**, 61-79 (1997).

11 Stevenson, D. J. in *Origin of the Earth* (ed H.E. Newsom and J.H. Jones) 231-249 (Oxford University Press, 1990).

12 Nakada, M. & Karato, S. Low viscosity of the bottom of the Earth's mantle inferred from the analysis of Chandler wobble and tidal deformation. *Physics of the Earth and Planetary Interiors* **192/193**, 68-80 (2012).

13 Peltier, W. R. Postglacial variation in the level of the sea: implications for climate dynamics and solid-Earth geophysics. *Review of Geophysics* **36**, 603-689 (1998).

14 Solomatov, V. S., El-Khozondar, R. & Tikare, V. Grain size in the lower mantle: constraints from numerical modeling of grain growth in two-phase systems. *Physics of the Earth and Planetary Interiors* **129**, 265-282 (2002).

15 Yamazaki, D., Kato, T., Ohtani, E. & Toriumi, M. Grain growth rates of $MgSiO_3$ perovskite and periclase under lower mantle conditions. *Science* **274**, 2052-2054 (1996).

16 O'Connell, R. J. & Budianski, B. Viscoelastic properties of fluid-saturated cracked solids. *Journal of Geophysical Research* **82**, 5719-5735 (1977).

17 Takei, Y. Effect of pore geometry on Vp/Vs: From equilibrium geometry to crack. *Journal of Geophysical Research* **107**, 10.1029/2001JB000522 (2002).

18 Dziewonski, A. M. & Anderson, D. L. Preliminary reference Earth model. *Physics of Earth and Planetary Interiors* **25**, 297-356 (1981).
19 McLachlan, D. S., Blaszkiewicz, M. & Newnham, R. E. Electrical resistivity of composite. *Journal of the American Ceramic Society* **73**, 2187-2203 (1990).
20 Xu, Y., Shankland, T. J. & Poe, B. T. Laboratory-based electrical conductivity in the Earth's mantle. *Journal of Geophysical Research* **105**, 27865-27875 (2000).
21 Secco, R. A. & Schloessin, H. H. The electrical resistivity of solid and liquid Fe at pressures up to 7 GPa. *Journal of Geophysical Research* **94**, 5887-5894 (1989).
22 Holme, R. Electromagnetic core-mantle coupling-I. Explaining decadal changes in the length of day. *Geophysical Journal International* **132**, 176-180 (1998).
23 Buffett, B. A. Constraints on magnetic energy and mantle conductivity from the forced nutations of the Earth. *Journal of Geophysical Research* **97**, 19581-19597 (1992).